applied sciences

MDPI

Article

Dynamic Interactions between Parallel Grid-Forming Inverters in a Microgrid

Sulaiman Z. Almutairi

Electrical Engineering Department, College of Engineering, Prince Sattam bin Abdulaziz University, Alkharj 11942, Saudi Arabia; s.almutairi@psau.edu.sa

Abstract: The potential instability issues caused by the dynamic interactions between parallel grid-forming inverters are examined. The approach adopted for analysis is *s*-domain admittance-based eigenvalue and mode shape analysis. This admittance is based on a five-node circuit diagram after the conversion of each electric circuit element and inverter control unit into impedance models. Eigenvalue analysis results show that unstable resonance modes may exist due to the interactions of two parallel inverters. Impacts of transmission line length, the converter control's virtual impedance unit, and the voltage feed-forward unit are examined via the eigenvalue and mode shape analysis. The results show that the virtual impedance control has a negligible influence on the resonance while the voltage feed-forward unit stabilizes the resonance. Finally, the stability analysis is validated using electromagnetic transient (EMT) simulations.

Keywords: grid-forming inverters; microgrids; impedance models; nodal admittance; eigenvalue analysis; mode shape analysis

Citation: Almutairi, S.Z. Dynamic Interactions between Parallel Grid-Forming Inverters in a Microgrid. *Appl. Sci.* **2023**, *13*, 6989. https://doi.org/10.3390/app13126989

Academic Editors: Luis Hernández-Callejo, Jiefeng Hu, Adrian Ioinovici, Josep M. Guerrero, Yinghao Shan and Zilin Li

Received: 16 April 2023
Revised: 23 May 2023
Accepted: 7 June 2023
Published: 9 June 2023

1. Introduction

The generation of electricity from eco-friendly sources is of significant interest worldwide, as there is an increasing integration of renewable energy into the power system [1]. A microgrid is a system that combines distributed renewable energy resources to function either independently as a stand-alone grid or as a single unit connected to the main grid [2,3]. There are various types of microgrids, including AC, DC, or hybrid AC/DC configurations.

An AC microgrid is a small-scale power system operating on alternating current (AC), which can function autonomously or in conjunction with an existing utility power grid. Both AC and DC microgrids provide distinct benefits and drawbacks, making it essential to consider the specific application and local conditions when selecting between them [4].

To ensure the safe and synchronized operation of microgrids, appropriate control is necessary. This involves managing the grid source, distributed energy resources, and distributed loads in an islanded microgrid, where grid-forming control is often employed for inverter-based resources (IBRs). Moreover, proper power-sharing between parallel inverters is essential. This is typically achieved through a real power/frequency (P-f) and reactive power/voltage (Q-V) droop control strategy, which governs the frequency and output voltage of the inverter by adjusting the output real and reactive power [5,6].

The droop control strategy is inspired by the characteristics of synchronous generators. However, a high R/X ratio of low-voltage (LV) distribution lines can lead to power coupling issues. To address such concerns, numerous enhanced droop-based power control methods have been suggested [5]. One of the promising solutions is employing virtual output impedance, which has demonstrated excellent performance in managing these challenges [7].

The dynamic interaction between multiple devices has been seen in the past. For example, interaction between Flexible AC Transmission System (FACTS) controllers has been observed [8–10]. Examples of FACTS devices are the Static Var Compensator (SVC)

and the Static Synchronous Compensator (STATCOM). In [9], a study case for SVC–SVC interaction is investigated. Based on the findings, both devices can adversely interact with each other depending on the grid conditions. In the case of high short-circuit ratio conditions, the effect of one SVC on the other SVC is not a concern. However, the effect is more pronounced if the short-circuit ratio is low.

Another example of adverse interaction is between FACTS devices and High-Voltage DC (HVDC) systems [10]. The results in [10] indicate that no control interactions have been observed between SVC and HVDC if the grid is strong or the short-circuit ratio is high. In the case of a weak grid, however, the effect is strong. With the increasing number of voltage source converters (VSCs), dynamic interaction among VSCs may pose stability problems. Several real-world stability issues are listed in [11–13]. The dynamic interaction among VSCs can be organized as:

- Interaction between similar VSCs, e.g., multi-parallel PV [11,12,14];
- Interaction between VSCs of a dissimilar kind, e.g., wind and STATCOM [13], Wind, and HVDC [15].

The multi-parallel inveters are coupled and influence each other due to grid impedance. In [16], the results indicated that when there are N paralleled inverters connected to the same PCC, each inverter will see the equivalent grid impedance amplified by N times the actual value. This indication illustrates why the VSCs do not behave as expected when they are connected in parallel, even when their specifications to operate individually are satisfied [17].

Another type of interaction is the converter–converter interaction when the converters are electrically close to each other. For this type of interaction, the stability issue occurs when the controls of the converters interact with each other. For example, when there is a step change in voltage, each will try to control and set the voltage to its reference value. However, since each converter control has different gain parameters and control speed, this probably could cause voltage oscillation.

Several real world issues have been reported in [11,12] regarding multi-parallel inverters. In [11], resonant issues were observed in a Dutch network with high penetration of PV inverters. Several unstable operation records of PV plants are presented in [12]. One case is a PV plant connected to utilities and containing 30 inverters operating in parallel. No local load is supplied. Based on the inverter specifications, the total harmonic distortion is below 2% at rated power. As it can be observed from the event, the current becomes highly distorted. Because of the instability, the PV inverters restart and restore normal operation. FFT analysis shows the 7th harmonic current magnitude at 20% of its rated current. Another case is described in [12] where PV plants shut down their inverters partially because of oscillations. In both cases, there was no reported outage or fault in the system that could be the cause of such incidents.

In West China, an SSO event occurred due to dynamic interaction between DFIG wind and STATCOM [13]. The event occurred in the Guohua area between the DFIG-based wind and STATCOM. From the recorded voltage waveforms during the event, three stages were experienced. After a small disturbance, 37 Hz voltage oscillations were observed in the first stage. At the second stage, due to voltage oscillation, harmonic reactive power from STATCOMs decreased. Then, oscillation increased and led to a trip of the wind farms.

The existing stability analysis regarding the parallel inverters primarily focuses on evaluating the small-signal behavior of the droop control scheme adopted [18–21]. In these studies, the interaction analysis of the current and the voltage controls are ignored or simplified since the bandwidth of the droop control loop and the voltage-current control loops are well separated [22,23]. Therefore, the dynamic interaction between the outer voltage loop, inner control loop, and the remaining system dynamics is overlooked. Such interaction may lead to instability issues at a higher frequency, as shown in [23].

Several techniques for analyzing stability have been proposed in the literature. The traditional state-space method, which is ideal for linear time-invariant structures, can be used [24]. The stability of the electric network is judged based on the system matrix,

notated as A. The system will be stable if all of A's eigenvalues are found in the left half-plane (LHP).

Building a state-space LTI model is not as straightforward as building an s-domain model. Therefore, in the current literature, building s-domain impedance models and evaluating stability via the s-domain models is another viable path. In [25], the s-domain nodal admittance matrix ($Y(s)$) was proposed to be used for eigenvalue analysis in 1999. The method is further developed in [26–28]. The method is based on the fact that the system stability could be judged by the zeros of the determinant of $Y(s)$, also known as the system eigenvalues. Furthermore, using the admittance matrix, we may identify the influencing factors using the branch current or the nodal voltage participation factor in [29].

This paper aims to analyze the dynamic interactions of two parallel grid-forming voltage-source converters and identify potential unstable oscillation modes and influencing factors. The study utilizes admittance-based eigenvalue and mode shape analysis, examining the effects of circuit impedance, virtual impedance unit, and voltage feed-forward unit. The accuracy of the findings is validated through electromagnetic transient (EMT) simulations.

The analysis method utilized in this study takes full advantage of the derived modular impedance blocks by formulating a five-node system admittance network for eigenvalue and mode shape analysis. By analyzing the mode shape of five nodal voltages, the study can pinpoint the influencing factors responsible for oscillation modes with high accuracy. In comparison, the conventional frequency-domain Nyquist stability method adopted in [22] provides limited accuracy since it agglomerates each inverter and its filter into a single block, leaving no room to pinpoint influencing factors accurately.

Taken together, this study's approach is significantly more advantageous than the conventional method, providing more precise analysis without the limitations of the conventional method.

Structure of the paper: The remainder of the paper is structured as follows. The microgrid topology and the overall grid-forming control configuration are presented in Section 2. The impedance derivations and the impedance models are presented Section 3. Admittance-based eigenvalue analyses are presented in Section 4. Section 4 also presents the mode shape analysis results. Section 5 presents the EMT simulation results. The paper is concluded in Section 6.

2. Microgrid and Control Structure

The studied 400-V microgrid is presented in Figure 1. It has two voltage source converters (VSCs) operating in parallel, where they are connected through distribution feeders and supply a common load. The DC sources are assumed to be constant DC voltage sources.

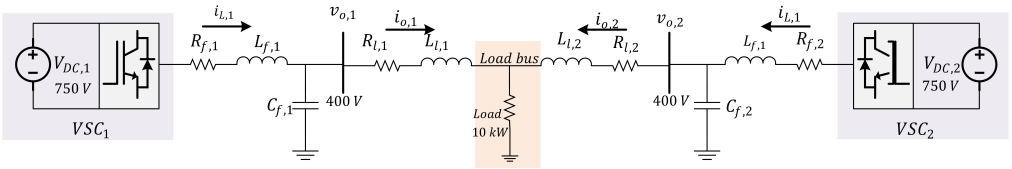

Figure 1. The system structure.

Figure 2 presents the control structure of the i-th VSC ($i = 1, 2$). The control is based on grid-forming control with the conventional droop control loop. The proportional current controller is adopted for the inner current control, whereas the proportional resonant (PR) controller is adopted in the voltage control loop. The system parameters are given in Table 1.

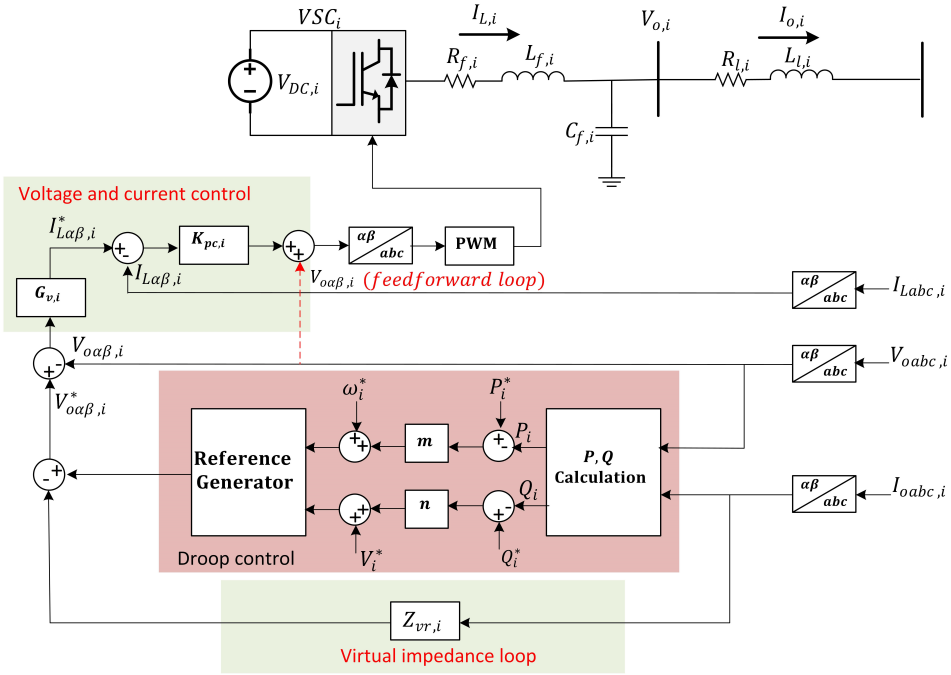

Figure 2. Control structure for the i-th VSC ($i = 1, 2$).

Table 1. System parameters.

Description	Parameters	Value
Rated power	S_b	10 kW
Rated voltage	V_b	400 V
Converter filter	$R_{f,i}$	0.1 Ω
	$L_{f,i}$	1.5 mH
	$C_{f,i}$	25 μF
Distribution feeder (Z_l, i)	$L_{l,i}$	0.45 mH
	R/X ratio	3
Local load (Z_L)	R_{load}	80 Ω
Sampling period	T_{si}	10^{-4}
Current control	$K_{pc,i}$	5
PR voltage control	$K_{pv,i}$	0.06
	$K_{rv,i}$	10
	$\omega_{c,i}$	8 rad/s
	ω_o	120 π rad/s
P-f droop	m_i	10^{-5}
V-Q droop	n_i	10^{-5}

3. Impedance Derivation

In the impedance model derivation, the droop controls are ignored. The impedance is derived firstly by assuming that the virtual impedance unit and the feed-forward unit are not applied, and then by including the two units.

Based on Figure 2, the LC-filter output can be modeled by a two-input, two-output model. This model has been derived in [22] by assuming the inverter output voltage and

the current flowing to the load as two inputs, while the converter current flowing to the point of the common coupling (PCC) bus and the PCC bus voltage are two outputs.

$$\begin{bmatrix} I_{L,i}(s) \\ V_{o,i}(s) \end{bmatrix} = \begin{bmatrix} G_{Io,i}(s) & Y_{L,i}(s) \\ -Z_{o,i}(s) & G_{Vo,i}(s) \end{bmatrix} \begin{bmatrix} I_{o,i}(s) \\ V_{PWM,i}(s) \end{bmatrix} \tag{1}$$

$$G_{Io,i}(s) = \frac{Z_{C_f,i}(s)}{Z_{L_f,i}(s) + Z_{C_f,i}(s)}, Y_{L,i}(s) = \frac{1}{Z_{L_f,i}(s) + Z_{C_f,i}(s)} \tag{2}$$

$$Z_{o,i}(s) = \frac{Z_{L_f,i}(s) Z_{C_f,i}(s)}{Z_{L_f,i}(s) + Z_{C_f,i}(s)}, G_{Vo,i}(s) = \frac{Z_{C_f,i}(s)}{Z_{L_f,i}(s) + Z_{C_f,i}(s)} \tag{3}$$

where $V_{PWM,i}(s)$ is the i-th inverter output voltage, and $Z_{L_f,i}(s)$ and $Z_{C_f,i}(s)$ are the impedance of the inductor and capacitor filter, respectively. Based on (1), the inner current control loop can be simplified as presented in Figure 3.

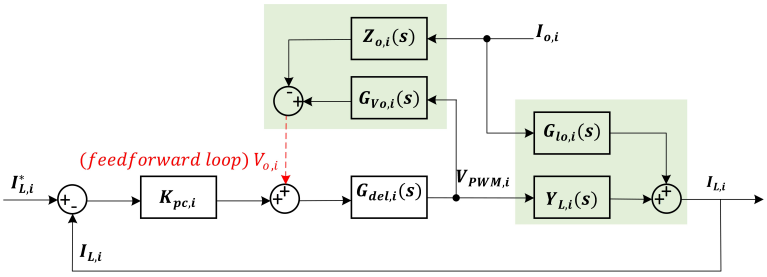

Figure 3. Simplified structure for the inner current control.

The inner loop dynamic can be obtained as follows:

$$I_{L,i}(s) = G_{cl,i}(s) I^*_{L,i}(s) + G_{Ioc,i}(s) I_{o,i}(s) \tag{4}$$

where $G_{cl,i}(s)$ is the closed-loop transfer function of the current controller, and $G_{Ioc,i}$ is the load current closed-loop transfer function. They are given as:

$$G_{cI,i}(s) = \frac{T_{c,i}(s)}{1 + T_{c,i}(s)}, \; G_{Ioc,i}(s) = \frac{G_{Io,i}(s)}{1 + T_{c,i}(s)} \tag{5}$$

where the open-loop gain of the inner loop is denoted by $T_{c,i}(s)$, and $G_{del,i}(s)$ is the approximated switching delay:

$$T_{c,i}(s) = K_{pc,i} G_{del,i}(s) Y_{L,i}(s), \tag{6}$$

and

$$G_{del,i}(s) = e^{-1.5 T_s s}. \tag{7}$$

The outer and the inner loop control can be simplified as in Figure 4. Therefore, the output voltage control can be described as follows

$$V_{o,i}(s) = G_{clv,i} V^*_{o,i}(s) - Z_{ov,i}(s) I_{o,i}(s), \tag{8}$$

$$G_{clv,i}(s) = \frac{T_{v,i}(s)}{1 + T_{v,i}(s)}, \; Z_{ov,i}(s) = \frac{Z_{C_f,i}(s)}{1 + T_{v,i}(s)} (1 - G_{Ioc,i}, (s)), \; T_{v,i}(s) = G_{v,i}(s) G_{cl,i}(s) Z_{C_f,i}(s) \tag{9}$$

where $G_{clv,i}(s)$ is the closed-loop transfer function of the outer-loop control, $Z_{ov,i}(s)$ is the output impedance transfer function, and $T_{v,i}(s)$ is open-loop gain of the outer-loop control. $G_{v,i}$ is the PR controller transfer function, which is given by

$$G_{v,i}(s) = K_{pv,i} + \frac{K_{rv,i}\omega_{c,i}s}{s^2 + \omega_{c,i}s + \omega_0^2} \tag{10}$$

Based on (8), the circuit model of the parallel VSCs serving a load can be built and is shown in Figure 5.

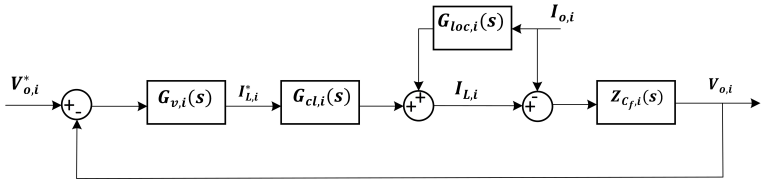

Figure 4. Simplified structure for the outer and inner control.

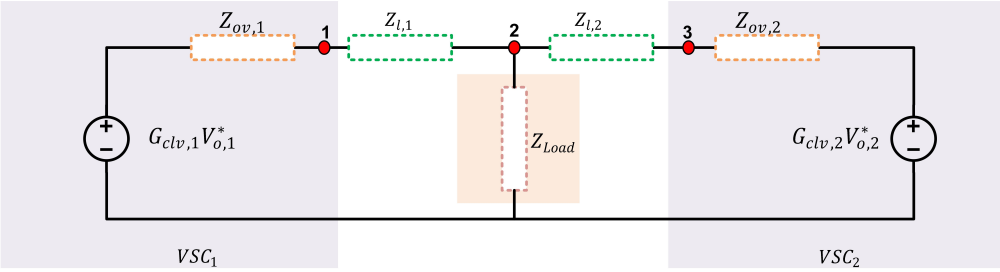

Figure 5. The circuit model of the parallel VSCs (without the feed-forward and the virtual impedance loops).

If the virtual impedance is considered $Z_{vr,i}(s)$, the voltage control becomes as follows:

$$V_{o,i}(s) = G_{clv,i}(s)V^*_{o,i}(s) - (Z_{ov,i}(s) + G_{clv,i}(s)Z_{vr,i}(s))I_{o,i}(s). \tag{11}$$

Therefore, the output impedance with virtual impedance in place is

$$Z_{tov,i}(s) = Z_{ov,i}(s) + G_{clv,i}(s)Z_{vr,i}(s). \tag{12}$$

It can be observed that adding the virtual impedance has no influence on the inner control loop.

Finally, considering the feed-forward unit, the dynamic behavior of the inner loop is changed as follows:

$$T'_{c,i}(s) = \frac{T_{c,i}(s)}{1 - G_{Vo,i}(s)G_{del,i}(s)}, \tag{13}$$

$$G'_{cl,i}(s) = \frac{T'_{c,i}(s)}{1 + T_{c,i}(s)}, \tag{14}$$

$$G'_{Ioc,i}(s) = \frac{G_{Io,i}(s)}{1 + T_{c,i}(s)} - \frac{Z_{o,i}(s)G_{del,i}(s)Y_{L,i}(s)}{(1 + T'_{c,i}(s))(1 - G_{del,i}(s)G_{Vo,i}(s))}. \tag{15}$$

If we substitute (13)–(15) into (9), the output voltage control behavior becomes

$$V_{o,i}(s) = G'_{clv,i}V^*_{o,i}(s) - Z'_{ov,i}(s)I_{o,i}(s) \tag{16}$$

$$\text{where } G'_{clv,i}(s) = \frac{T'_{v,i}(s)}{1 + T'_{v,i}(s)}, Z'_{ov,i}(s) = \frac{Z_{C_f,i}(s)}{1 + T'_{v,i}(s)}(1 - G'_{Ioc,i}(s)), \tag{17}$$

$$T'_{v,i}(s) = G_{v,i}(s)G'_{cl,i}(s)Z_{C_f,i}(s). \quad (18)$$

As can be seen, adding the feed-forward unit has an impact on both the inner control loop and the output impedance, unlike the virtual impedance unit.

Based on the derived models in (11) and (16), a five-node circuit model can be built as shown in Figure 6.

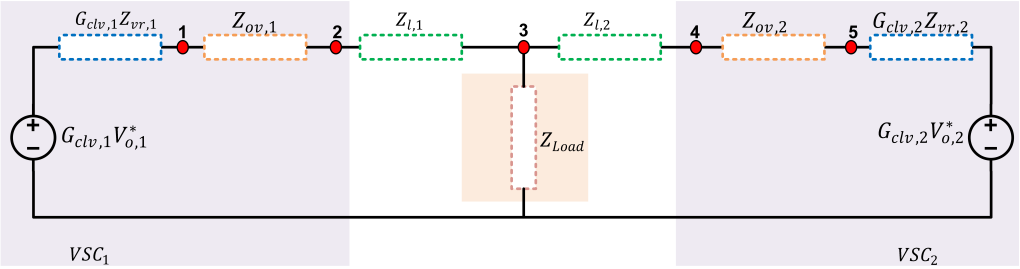

Figure 6. The five-node circuit model of the parallel VSCs serving a load (with the feed-forward and the virtual impedance loops).

4. Stability Analysis

4.1. Eigenvalue-Based Stability Analysis Using s-Domain Nodal Admittance Matrix

For a general AC electric network, the nodal voltage equation in the *s*-domain can be given as follows [30]

$$I^n(s) = Y(s)V^n(s) \quad (19)$$

where $Y(s)$ is the nodal admittance matrix, and $V^n(s)$ and $I^n(s)$ are the vectors of nodal voltages and injected currents to the nodes, respectively.

The system eigenvalues can be obtained by the nodal admittance matrix. According to [25,28], the zeros of the determinant of $Y(s)$ are equal to its eigenvalues. Based on that, the system eigenvalues can be identified by finding the zeros of the following equation

$$\det[Y(s)] = 0 \quad (20)$$

where det[] is the function to compute the determinant of the enclosed matrix.

4.2. Influencing Factor Identification

The influencing factor for a certain oscillation mode is determined using two indices: the nodal voltage mode shape analysis and the participation factor. The analysis can be conducted by using the nodal admittance matrix. The analysis can be applied to determine each node's contribution to an oscillation mode [31].

- *Nodal voltage mode shape*

Assuming that the eigenvalue of the q-th oscillation mode of the system is s_q and letting $s = s_q$, the following is true: $\det[Y(s_q)] = 0$. Since the determinant of $Y(s_q)$ is equal to zero, one of its eigenvalues must equal zero (for illustration, let $\lambda_1 = 0$). $Y(s_q)$ can be factorized via eigenvalue decomposition [32]:

$$Y(s_q) = Q\Lambda Q^{-1} \quad (21)$$

where $\Lambda = \text{diag}(\lambda_1, \lambda_2, ..., \lambda_n)$ is a diagonal matrix containing the eigenvalues of $Y(s_q)$, $Q = [Q_1, Q_2, ..., Q_n]$ is the left eigenvector matrix, and Q^{-1} is the right eigenvector matrix.

Substituting (21) into (19) leads to the following

$$Q^{-1}V^n(s_q) = \Lambda^{-1}Q^{-1}I^n(s_q) \quad (22)$$

Defining the modal voltage as

$$U = Q^{-1}V^n(s_q), \tag{23}$$

and the modal current as

$$J = Q^{-1}I^n(s_q), \tag{24}$$

then the above equation can be rewritten as

$$U = \Lambda^{-1}J, \tag{25}$$

or

$$\begin{bmatrix} U_1 \\ U_2 \\ \vdots \\ U_n \end{bmatrix} = \begin{bmatrix} \lambda_1^{-1} & & & \\ & \lambda_2^{-1} & & \\ & & \ddots & \\ & & & \lambda_n^{-1} \end{bmatrix} \begin{bmatrix} J_1 \\ J_2 \\ \vdots \\ J_n \end{bmatrix}. \tag{26}$$

Since $\lambda_1^{-1} = \infty$, U_1 has a larger value than U_m $(m = 2, \ldots, n)$. Therefore, Equation (23) can be represented as

$$V^n(s_q) = QU. \tag{27}$$

Based on that, Q_1 can be described as the nodal voltage mode shape of the q-th oscillation mode, which can be used to examine each node's contribution to the eigenvalue λ_1.

The influencing factors can be determined using the nodal voltage mode shape. Some elements in Q_1 might have clearly greater magnitudes than the others, implying that the correlated nodes are significantly more relevant and can be identified as influencing factors on the q-th oscillation mode.

- *Participation Factor:*

Similarly, the participation factor (PF) can be obtained using the nodal admittance matrix. As with our previous assumption, let $s = s_q$, then, $Y(s_q)$ is diagonalized as in (21). The zero eigenvalue (for example, λ_1) is found, and then the participation factor can be computed as

$$PF^n = \mid Q_{n1}Q_{1n}^{-1} \mid \Big/ \sum_{m=1}^{N} \mid Q_{m1}Q_{1m}^{-1} \mid \tag{28}$$

where N is the number of nodes and Q_{m1} and $Q^{-}1_{1m}$ are elements of the Q matrix.

4.3. Nodal Admittance Matrix Calculation

The derivation of $Y(s)$ is based on constructing the nodal admittance matrix, which is explained in great detail in [33]. First, $Y(s)$ is constructed assuming the control has no virtual impedance nor the voltage feed-forward loops. Therefore, the nodal admittance matrix of Figure 5 becomes a 3×3 matrix given by

$$Y(s) = \begin{bmatrix} Y_{ov,1}(s) + Y_{l,1}(s) & -Y_{l,1}(s) & 0 \\ -Y_{l,1}(s) & Y_{l,1}(s) + Y_{Load}(s) + Y_{l,2}(s) & -Y_{l,2}(s) \\ 0 & -Y_{l,2}(s) & Y_{ov,2}(s) + Y_{l,2}(s) \end{bmatrix} \tag{29}$$

where $Y_{ov,i}(s) = \frac{1}{Z_{ov,i}(s)}$, $Y_{l,i}(s) = \frac{1}{Z_{l,i}(s)}$, and $Y_{Load}(s) = \frac{1}{Z_{Load}(s)}$

If we consider adding the virtual impedance and the voltage feed-forward loops, $Y(s)$ will have five nodes and can be written as follows:

$$Y(s) = \begin{bmatrix} Y_{vr,1}(s) + Y_{ov,1}(s) & -Y_{ov,1}(s) & 0 & 0 & 0 \\ -Y_{ov,1}(s) & Y_{ov,1}(s) + Y_{l,1}(s) & -Y_{l,1}(s) & 0 & 0 \\ 0 & -Y_{l,1}(s) & Y_{l,1}(s) + Y_{\text{Load}}(s) + Y_{l,2}(s) & -Y_{l,2}(s) & 0 \\ 0 & 0 & -Y_{l,2}(s) & Y_{ov,2}(s) + Y_{l,2}(s) & -Y_{ov,2}(s) \\ 0 & 0 & 0 & -Y_{ov,2}(s) & Y_{ov,2}(s) + Y_{vr,2}(s) \end{bmatrix} \quad (30)$$

where $Y_{vr,i}(s) = \frac{1}{G_{clv,i} Z_{vr,i}}$.

Once the $Y(s)$ matrix is constructed, the stability analysis can be applied.

4.4. Eigenvalue Analysis

The eigenvalue analysis is performed using $Y(s)$ of the system. MATLAB command `tfzero` can lead to all zeros of $Y(s)$.

First, a single VSC connected to a load (the other VSC is disconnected) is considered. Figure 7a shows the eigenvalues of a single VSC connected to a load. As can be seen, the system is stable. Figure 7b shows the eigenvalues when the two VSCs are operating in parallel. Two pairs of the eigenvalue are introduced in the right half-plane (RHP). The system becomes unstable. Therefore, although a stable operation of a single inverter is observed, the interaction between the parallel-inverter could lead to instability.

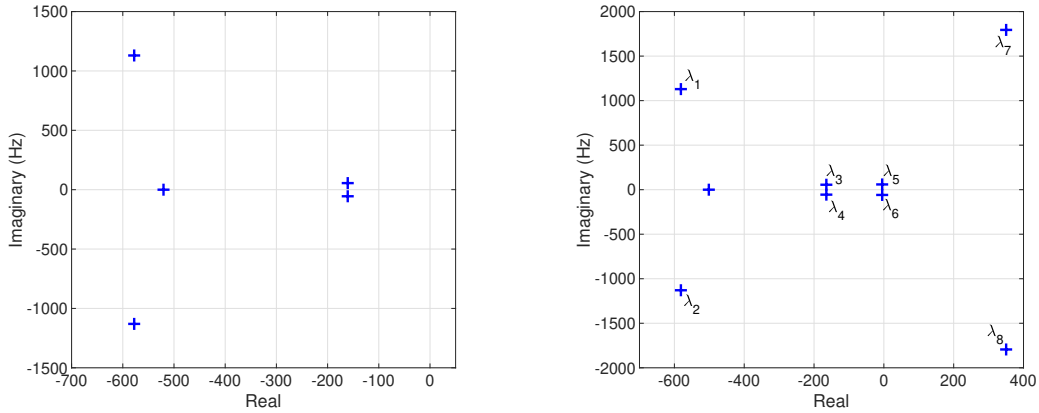

(**a**) (**b**)

Figure 7. (**a**) Eigenvalues of a single VSC connected to a load. The system is stable. (**b**) Eigenvalues of the paralleled VSCs system. Two pairs of the eigenvalue are introduced at the RHP. The system is unstable. The four modes are: $\lambda_{1,2}$ at 1130 Hz, $\lambda_{3,4}$ at 57 Hz, $\lambda_{5,6}$ at 60 Hz, $\lambda_{7,8}$ at 1750 Hz.

Figure 8a presents the eigenvalues of the parallel VSCs with different distribution line impedance. It is evident that increasing the line impedance improves the system's stability. This observation indicates that the undesired resonance can be prevented by adjusting the impedances between the parallel VSCs. This can be done through changing inverter controls.

Based on (9), (12) and (17), there are two approaches that can be applied to change the VSC output impedance. They are:

1. Adding the virtual impedance;
2. Applying the feed-forward loop in the inner control.

The two approaches are investigated. Figure 8b shows the eigenvalues of the parallel VSCs when the virtual impedance loop is used. Different values are examined. Based on the results, it is clear that the virtual impedance has a slight influence on the resonant frequency. This indicates that the virtual impedance does not affect the stability of the system.

Figure 8c depicts the eigenvalues of the parallel VSCs when the feed-forward loop is added to the inner control. As can be seen from the results, it is obvious that the system becomes stable with no eigenvalue on the RHP. Therefore, adding the voltage feed-forward loop stabilizes the system.

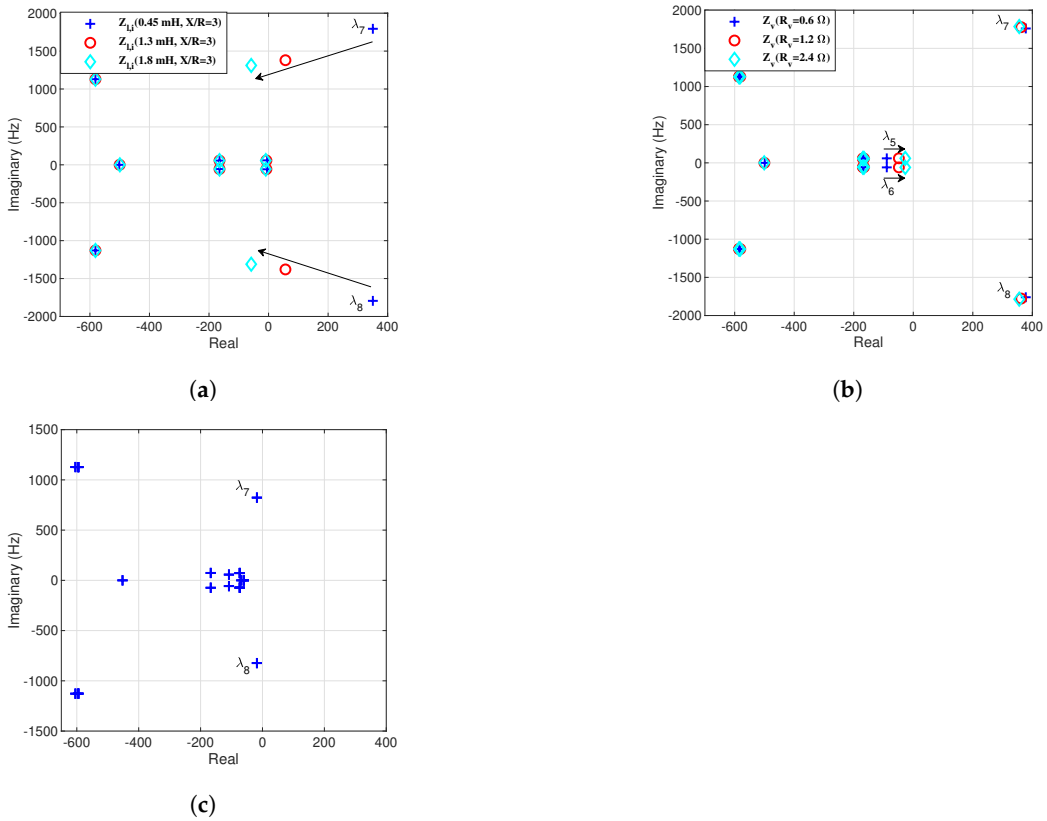

Figure 8. Eigenvalues of the paralleled VSC system. (**a**) The effect of different distribution line impedances. Increasing the line impedance improves the system's stability. (**b**) The effect of virtual impedance. There is no effect on the unstable modes. (**c**) The effect of voltage feed-forward control. The system becomes stable with voltage feed-forward.

4.5. Mode Shape Analysis

The nodal admittance matrix in (30) is further subjected to mode shape analysis as described in Section 4.2. The analysis helps to identify the contribution of each node to the resonance mode.

In Figure 9a–d, five nodal voltage mode shapes regarding $\lambda_{1,2}$, $\lambda_{3,4}$, $\lambda_{5,6}$, and $\lambda_{7,8}$ are presented.

For $\lambda_{1,2}$, nodes 2, 3, and 4 have larger nodal mode shapes than nodes 1 and 5. $\lambda_{3,4}$ have larger mode shapes at nodes 1 and 5. The nodal mode shapes in these two modes have similar phases for two inverters. They can be described as coherent modes where the two converters act as a whole.

For $\lambda_{5,6}$, nodes 1 and 5 have opposite phases. This means that this mode is due to inverter interactions. This observation matches the results in Figure 8b, where $\lambda_{5,6}$ values are moving when changing the virtual impedance values.

$\lambda_{7,8}$ is also an interaction mode where the two inverters are out of phase. Node 2 and 4 have more influence, while nodes 1, 3, and 5 have less influence. This observation confirms the eigenvalue analysis, which shows that the virtual impedance loop has a slight effect on the unstable mode $\lambda_{7,8}$.

For comparative studies, the nodal participation factor approach previously introduced in [29] is used. The results are shown in Table 2, and the participation factor is computed via (28). Based on the results, $\lambda_{1,2}$ is related to nodes 2, 3, and 4, $\lambda_{3,4}$ and $\lambda_{5,6}$ are related to nodes 1 and 5, and $\lambda_{7,8}$ is related to nodes 2 and 4. The observed results match the mode shape analysis in Figure 9. However, the participation factor cannot pinpoint which mode is coherent or interactive, whereas the nodal mode shape has this appealing ability.

Table 2. Participation factor analysis.

Node	$\lambda_{1,2}$	$\lambda_{3,4}$	$\lambda_{5,6}$	$\lambda_{7,8}$
1	0.0048	**0.5000**	**0.5006**	0.0020
2	**0.3341**	0.0000	0.0007	**0.4982**
3	**0.3333**	0.0000	0.0000	0.0000
4	**0.3341**	0.0000	0.0007	**0.4982**
5	0.0048	**0.5000**	**0.5006**	0.0020

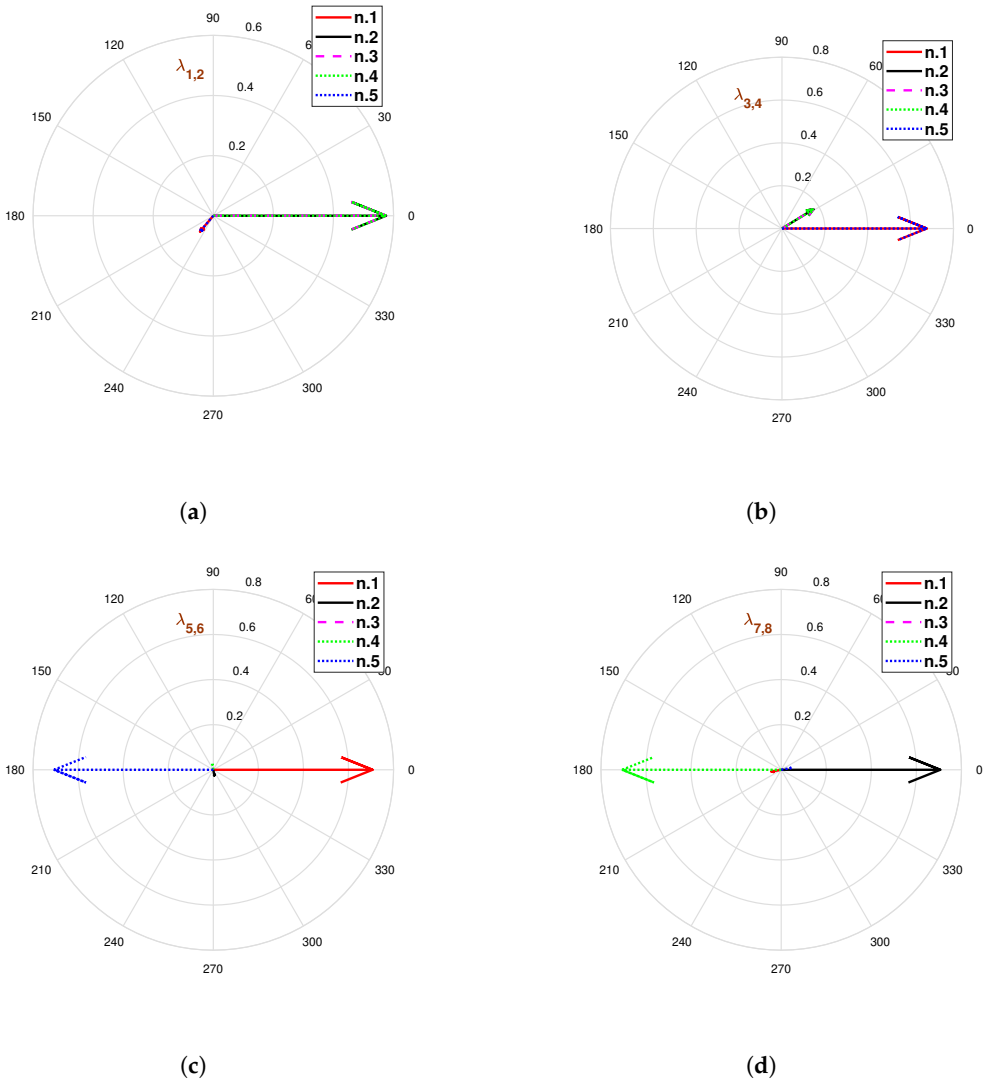

Figure 9. Mode shape analysis. (For $\lambda_{1,2}$ in (**a**) and $\lambda_{3,4}$ in (**b**), the mode shapes have close phases that are described as abrogated modes, since they are not influenced by any change in the system parameters or control as evident in Figure 8. For $\lambda_{5,6}$ in (**c**) and $\lambda_{7,8}$ in (**d**), they have opposite contributions based on their nodal mode shape. $\lambda_{5,6}$ is more effective at nodes 1 and 5, which matches the observation in Figure 8b. For $\lambda_{7,8}$, nodes 2 and 4 have more influence, while nodes 1, 3, and 5 have less influence.)

5. EMT Study

The above stability analysis is validated using time–domain simulation. The model in Figure 1 is built in MATLAB/SimPowerSystem with the parameters presented in Table 1. The load is considered to be 1 pu.

Figure 10 presents the dynamic responses of the output voltage $V_{abc,o}$, the current $I_{abc,L}$, and the exported power of a single VSC connected to the load (the other VSC is

disconnected). The results show the system is stable, which aligns with the eigenvalue analysis results in Figure 7a. Additionally, a load change (0.5 pu drop) is applied at $t = 1.2$ s. Once the load drops, the VSC automatically reduces its output power generation based on the load demand.

Figure 11 shows the the dynamic responses of the parallel VSCs without applying the feed-forward and the virtual impedance loops. As can been seen, the resonance arises when the VSCs are operating in parallel. The results match the observation in the eigenvalue analysis in Figure 7b.

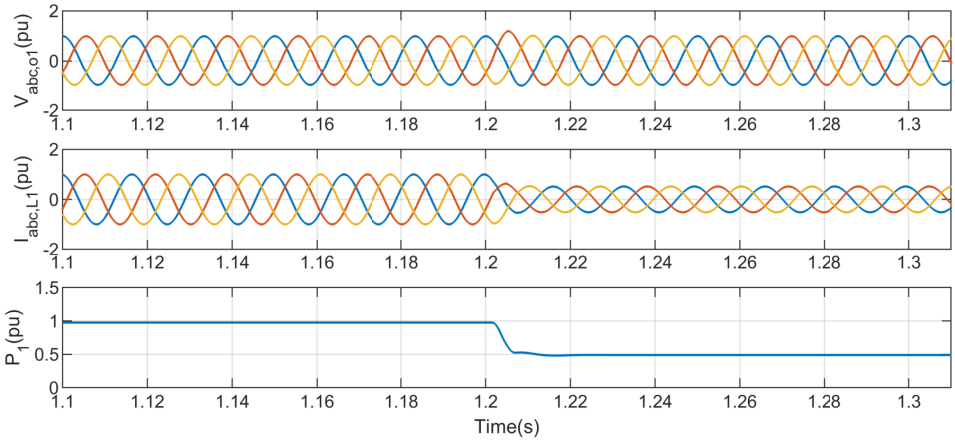

Figure 10. The output voltage $V_{abc,o}$, the current $I_{abc,L}$, and the exported power of a single VSC.

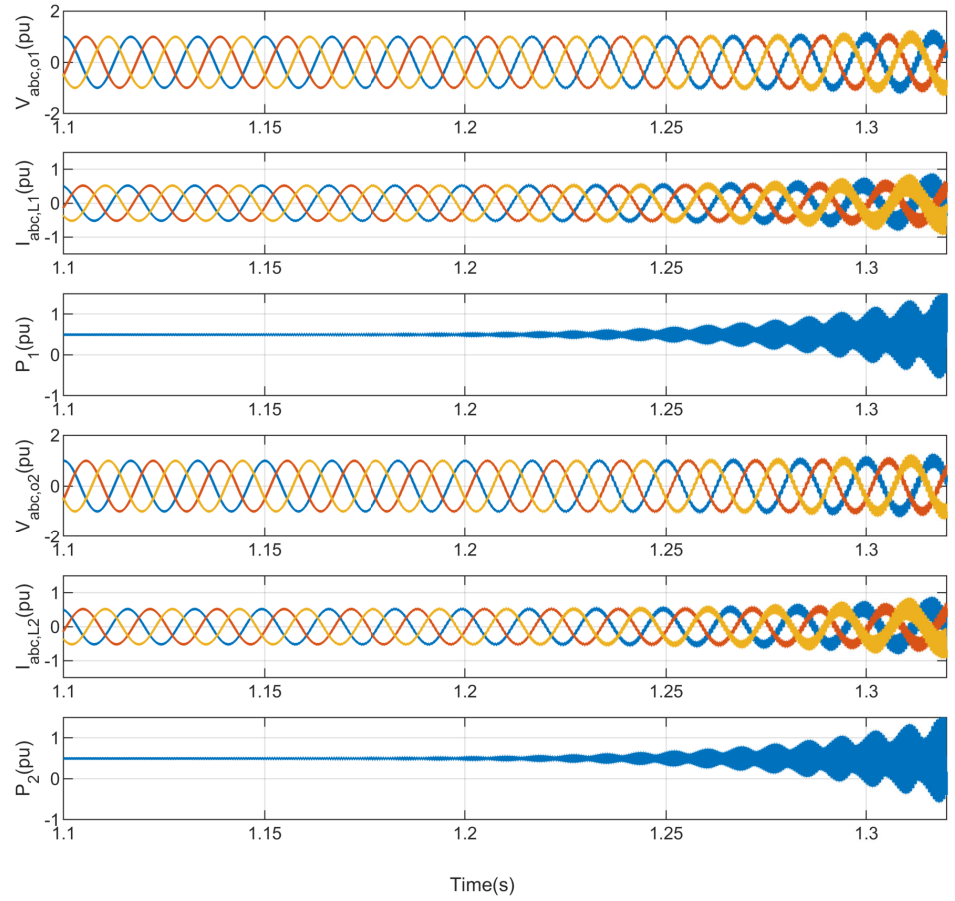

Figure 11. The output voltage $V_{abc,o}$, the current $I_{abc,L}$, and the exported power of the parallel VSCs without applying the feed-forward and the virtual impedance loops.

The dynamic responses of the parallel VSCs after increasing the distribution line impedance from $L_{l,i} = 0.45$ mH to $L_{l,i} = 1.8$ mH are presented in Figure 12. It is clear that the resonances disappear after increasing the line inductance, which matches the analysis in Figure 8a.

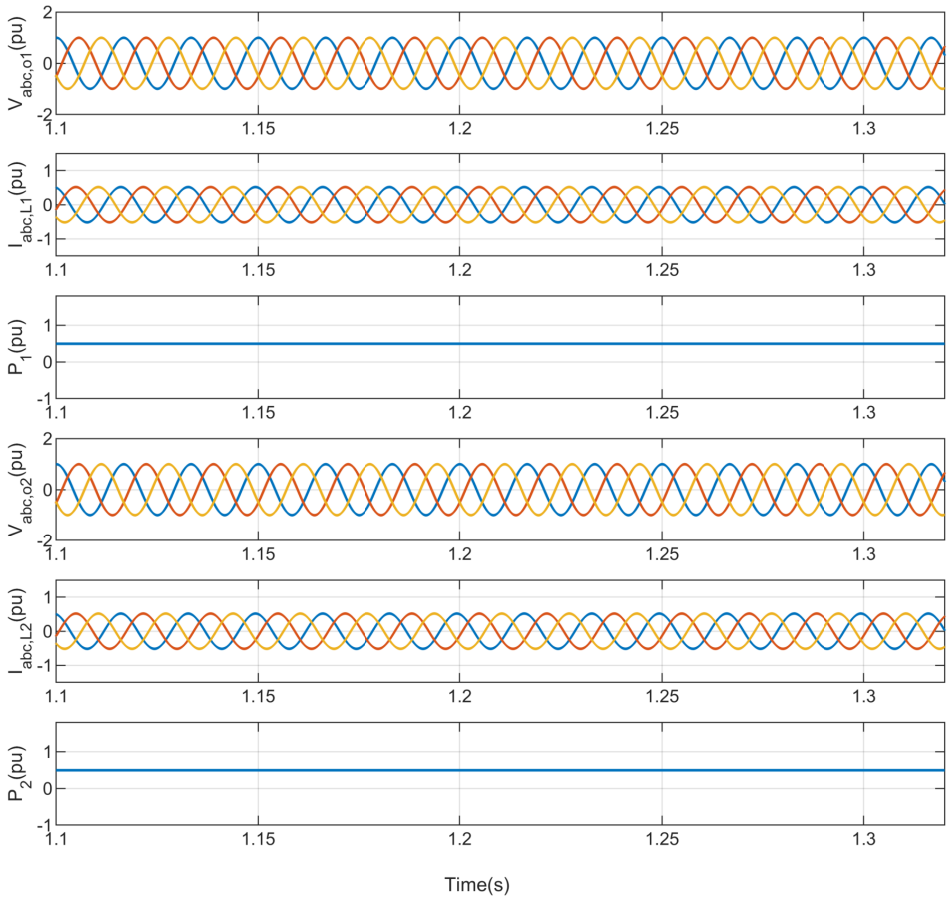

Figure 12. The output voltage $V_{abc,o}$, the current $I_{abc,L}$, and the exported power of the parallel VSCs with $L_{l,i} = 1.8$ mH.

Figure 13 presents the dynamic responses of the parallel VSCs after applying the virtual impedence loop. Based on the results, the resonances still exist, which validates the analysis in Figure 8b that the virtual impedance has a slight effect on damping such a resonance.

Finally, Figure 14 shows the dynamic responses of the parallel VSCs when the feed-forward loop is added in the inner control. It can be seen that the voltage feed-forward loop stabilizes the system and that the resonances are mitigated. The EMT results corroborate the analysis results shown in Figure 8c. Additionally, a load change (1.0 pu drop) is applied at $t = 1.2$ s. Both VSCs increase their output power to meet the load demand.

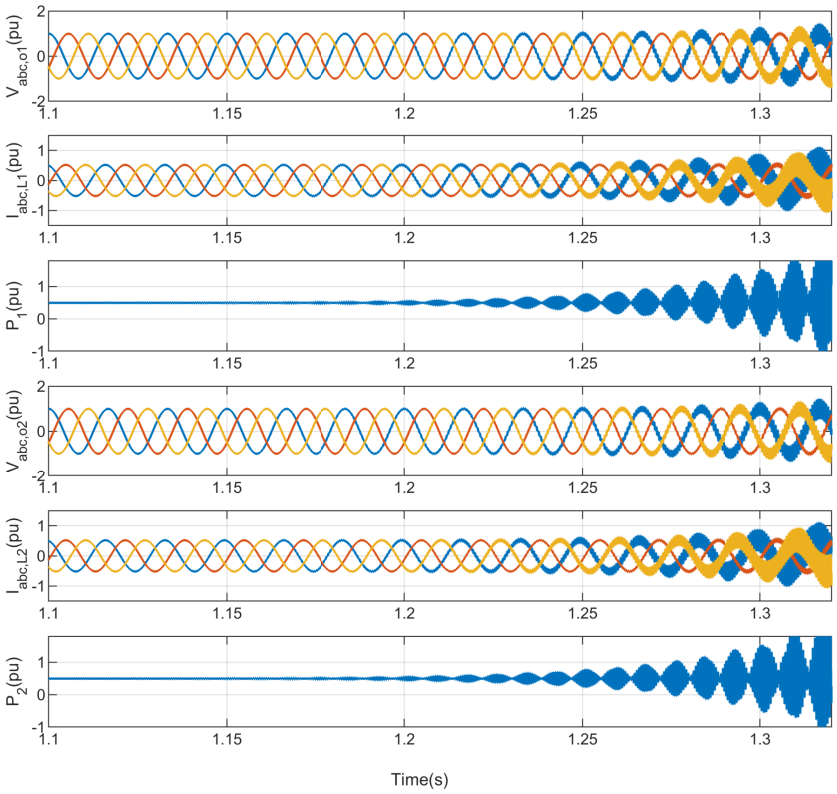

Figure 13. The output voltage $V_{abc,o}$, the current $I_{abc,L}$, and the exported power of the parallel VSCs when applying the virtual impedance loops.

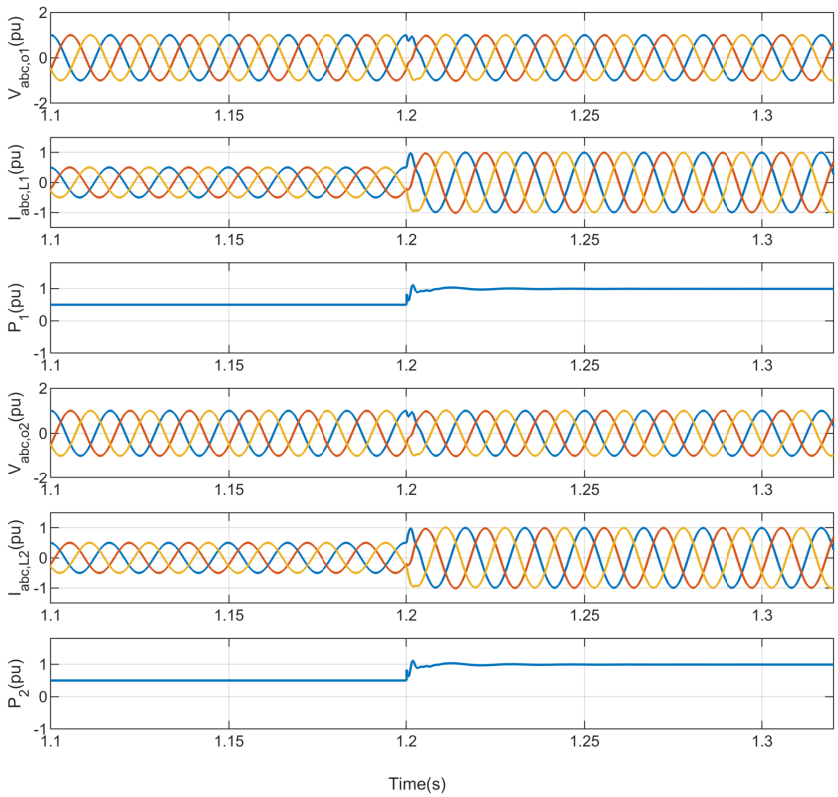

Figure 14. The output voltage $V_{abc,o}$, the current $I_{abc,L}$, and the exported power of the parallel VSCs when applying the feed-forward loops.

6. Conclusions

This paper studied the potential instability risks caused by the dynamic interactions between parallel grid-forming inverters. To shed light on the nature of undesirable resonances, the *s*-domain admittance-based analysis was performed on an islanded microgrid with two parallel inverters. When two inverters were operated in parallel, eigenvalue analysis showed that two unstable modes can exist. The eigenvalue and mode shape analysis were used to investigate the effect of the virtual impedance and the voltage feed-forward. The results show that virtual impedance has a slight influence at the resonant frequency, while adding the voltage feed-forward loop stabilizes the system and damps the resonances. Finally, the stability analysis is validated using EMT simulations. In our future work, we will review different grid-forming control strategies introduced in the literature. We will compare various performance aspects of grid-forming control techniques. We will explore the dynamic interactions between inverters with different control modes. According to the literature review, the existing studies mainly focus on the interactions between inverters that have the same control mode. Hybrid control interactions are rarely studied.

Funding: This project was funded by the Deanship of Scientific Research at Prince Sattam bin Abdulaziz University award number 2022/01/20089.

Data Availability Statement: The data that support the findings of this study are available within the article.

Conflicts of Interest: The author declares no conflict of interest.

References

1. Saha, S.; Saleem, M.; Roy, T. Impact of high penetration of renewable energy sources on grid frequency behaviour. *Int. J. Electr. Power Energy Syst.* **2023**, *145*, 108701. [CrossRef]
2. Jain, D.; Saxena, D. Comprehensive review on control schemes and stability investigation of hybrid AC-DC microgrid. *Electr. Power Syst. Res.* **2023**, *218*, 109182. [CrossRef]
3. Zheng, H.; Liu, Z.; An, R.; Liu, J.; Wu, T.; Lin, Z. An Islanding Detection Method Using Synchronized Small-AC-Signal Injection for Grid-Forming Inverters in Microgrids. *IEEE Trans. Power Electron.* **2023**, *38*, 5816–5831. [CrossRef]
4. Armghan, A.; Hassan, M.; Armghan, H.; Yang, M.; Alenezi, F.; Azeem, M.K.; Ali, N. Barrier Function Based Adaptive Sliding Mode Controller for a Hybrid AC/DC Microgrid Involving Multiple Renewables. *Appl. Sci.* **2021**, *11*, 8672. [CrossRef]
5. Mohammed, N.; Lashab, A.; Ciobotaru, M.; Guerrero, J.M. Accurate reactive power sharing strategy for droop-based islanded AC microgrids. *IEEE Trans. Ind. Electron.* **2022**, *70*, 2696–2707. [CrossRef]
6. Kikusato, H.; Orihara, D.; Hashimoto, J.; Takamatsu, T.; Oozeki, T.; Matsuura, T.; Miyazaki, S.; Hamada, H.; Miyazaki, T. Performance evaluation of grid-following and grid-forming inverters on frequency stability in low-inertia power systems by power hardware-in-the-loop testing. *Energy Rep.* **2023**, *9*, 381–392. [CrossRef]
7. Chiang, S.; Chang, J. Parallel control of the UPS inverters with frequency-dependent droop scheme. In Proceedings of the 2001 IEEE 32nd Annual Power Electronics Specialists Conference (IEEE Cat. No. 01CH37230), Vancouver, BC, Canada, 17–21 June 2001; IEEE: Piscataway, NJ, USA, 2001; Volume 2, pp. 957–961.
8. Kim, H.J.; Nam, T.; Hur, K.; Chang, B.; Chow, J.H.; Entriken, R. Dynamic interactions among multiple FACTS controllers—A survey. In Proceedings of the 2011 IEEE Power and Energy Society General Meeting, Detroit, MI, USA, 24–29 July 2011; pp. 1–8.
9. Pilotto, L.A.S.; Long, W.F.; Edris, A.A. Basic mechanisms of control interactions among power electronic-assisted power systems. In Proceedings of the 2001 IEEE/PES Transmission and Distribution Conference and Exposition, Developing New Perspectives (Cat. No.01CH37294), Atlanta, GA, USA, 2 November 2001; Volume 1, pp. 397–402.
10. Pilotto, L.; Ping, W.; Carvalho, A.; Wey, A.; Long, W. Analysis of Control Interactions on FACTS Assisted Power Systems. In *EPRI Research Project 3022–33.34: First Interim Report*; Electric Power Research Institute: Palo Alto, CA, USA, 1995.
11. Enslin, J.H.; Heskes, P.J. Harmonic-interaction between a large number of distributed power inverters and the distribution network. *IEEE Trans. Power Electron.* **2004**, *19*, 1586–1593. [CrossRef]
12. Li, C. Unstable Operation of Photovoltaic Inverter From Field Experiences. *IEEE Trans. Power Deliv.* **2018**, *33*, 1013–1015. [CrossRef]
13. Xu, Y.; Zhao, S.; Cao, Y.; Sun, K. Understanding Subsynchronous Oscillations in DFIG-Based Wind Farms Without Series Compensation. *IEEE Access* **2019**, *7*, 107201–107210. [CrossRef]
14. Ren, L.; Guo, H.; Dou, Z.; Wang, F.; Zhang, L. Modeling and Analysis of the Harmonic Interaction between Grid-Connected Inverter Clusters and the Utility Grid. *Energies* **2022**, *15*, 3490. [CrossRef]
15. Amin, M.; Molinas, M. Understanding the Origin of Oscillatory Phenomena Observed Between Wind Farms and HVdc Systems. *IEEE J. Emerg. Sel. Top. Power Electron.* **2017**, *5*, 378–392. [CrossRef]

16. Agorreta, J.L.; Borrega, M.; López, J.; Marroyo, L. Modeling and control of N-paralleled grid-connected inverters with LCL filter coupled due to grid impedance in PV plants. *IEEE Trans. Power Electron.* **2011**, *26*, 770–785. [CrossRef]
17. Lu, M.; Yang, Y.; Johnson, B.; Blaabjerg, F. An Interaction-Admittance Model for Multi-Inverter Grid-Connected Systems. *IEEE Trans. Power Electron.* **2019**, *34*, 7542–7557. [CrossRef]
18. Coelho, E.A.A.; Cortizo, P.C.; Garcia, P.F.D. Small-signal stability for parallel-connected inverters in stand-alone AC supply systems. *IEEE Trans. Ind. Appl.* **2002**, *38*, 533–542. [CrossRef]
19. Xiong, R.; Lee, Y.; Zhao, J. Modeling and analysis of stability for parallel inverters operated with instantaneous maximum current control strategy. In Proceedings of the Multiconference on "Computational Engineering in Systems Applications", Beijing, China, 4–6 October 2006; IEEE: Piscataway, NJ, USA, 2006; Volume 2, pp. 1701–1706.
20. Yu, K.; Ai, Q.; Wang, S.; Ni, J.; Lv, T. Analysis and Optimization of Droop Controller for Microgrid System Based on Small-Signal Dynamic Model. *IEEE Trans. Smart Grid* **2016**, *7*, 695–705. [CrossRef]
21. He, J.; Li, Y.W. Analysis, design, and implementation of virtual impedance for power electronics interfaced distributed generation. *IEEE Trans. Ind. Appl.* **2011**, *47*, 2525–2538. [CrossRef]
22. Wang, X.; Blaabjerg, F.; Chen, Z.; Wu, W. Resonance analysis in parallel voltage-controlled distributed generation inverters. In Proceedings of the 2013 Twenty-Eighth Annual IEEE Applied Power Electronics Conference and Exposition (APEC), Long Beach, CA, USA, 17–21 March 2013; IEEE: Piscataway, NJ, USA, 2013; pp. 2977–2983.
23. Corradini, L.; Mattavelli, P.; Corradin, M.; Polo, F. Analysis of parallel operation of uninterruptible power supplies loaded through long wiring cables. *IEEE Trans. Power Electron.* **2009**, *25*, 1046–1054. [CrossRef]
24. Kundur, P.S.; Malik, O.P. *Power System Stability and Control*; McGraw-Hill Education: New York, NY, USA, 2022.
25. Semlyen, A. S-domain methodology for assessing the small signal stability of complex systems in nonsinusoidal steady state. *IEEE Trans. Power Syst.* **1999**, *14*, 132–137. [CrossRef]
26. Gomes, S.; Martins, N.; Portela, C. Modal analysis applied to s-domain models of ac networks. In Proceedings of the 2001 IEEE Power Engineering Society Winter Meeting. Conference Proceedings (Cat. No. 01CH37194), Columbus, OH, USA, 28 January–1 February 2001; IEEE: Piscataway, NJ, USA, 2001; Volume 3, pp. 1305–1310.
27. Varricchio, S.L.; Gomes, S.; Martins, N. S-domain approach to reduce harmonic voltage distortions using sensitivity analysis. In Proceedings of the 2001 IEEE Power Engineering Society Winter Meeting, Conference Proceedings (Cat. No. 01CH37194), Columbus, OH, USA, 28 January–1 February 2001; IEEE: Piscataway, NJ, USA, 2001; Volume 2, pp. 809–814.
28. Varricchio, S.; Gomes, S., Jr. Electrical network dynamic models with application to modal analysis of harmonics. *Electr. Power Syst. Res.* **2018**, *154*, 433–443. [CrossRef]
29. Zhan, Y.; Xie, X.; Liu, H.; Liu, H.; Li, Y. Frequency-domain modal analysis of the oscillatory stability of power systems with high-penetration renewables. *IEEE Trans. Sustain. Energy* **2019**, *10*, 1534–1543. [CrossRef]
30. Boylestad, R.L. *Introductory Circuit Analysis*; Pearson Education India: Noida, India, 2003.
31. Xu, Z.; Wang, S.; Xing, F.; Xiao, H. Study on the method for analyzing electric network resonance stability. *Energies* **2018**, *11*, 646. [CrossRef]
32. Xu, W.; Huang, Z.; Cui, Y.; Wang, H. Harmonic resonance mode analysis. *IEEE Trans. Power Deliv.* **2005**, *20*, 1182–1190. [CrossRef]
33. Grainger, J.J. *Power System Analysis*; McGraw-Hill: New York, NY, USA, 1999.